AIAA JOURNAL
Vol. 30, No. 2, February 1992

Experimental Investigation of Turbulent Flow Through a Circular-to-Rectangular Transition Duct

D. O. Davis* and F. B. Gessner†
University of Washington, Seattle, Washington 98195

An experimental study was conducted to investigate incompressible turbulent flow through a circular-to-rectangular transition duct having the same inlet and outlet cross-sectional areas, an overall length-to-diameter ratio of 4.5, and an aspect ratio of 3.0 at the exit plane. Downstream of the inlet, the local cross-sectional area increased to a value 15% above the inlet value and then decreased to the exit value. Mean flow and turbulence data were obtained by means of pressure probe and hot-wire instrumentation for an operating bulk Reynolds number of 3.9×10^5. The results show that curvature of the duct walls induces a relatively strong pressure-driven crossflow that develops into a contrarotating vortex pair near the diverging side walls of the duct. This vortex pair significantly distorts both the primary mean velocity and Reynolds stress fields. Law-of-the-wall behavior was observed in the near-wall region at the duct exit plane and, to a lesser extent, immediately after the end of transition. Analysis of the results shows that caution must be observed if conventional wall functions are used to predict the present flow situation.

Nomenclature

a = semimajor axis of superellipse
B = blockage factor, $(2\delta_1/R)$
b = semiminor axis of superellipse
C = law-of-the-wall constant, 5.0
C_f = skin-friction coefficient, $[\tau_w/(\frac{1}{2}\rho U_b^2)]$
C_p = pressure coefficient, $[(P_w - P_i)/(\frac{1}{2}\rho U_b^2)]$
C_μ = empirical coefficient, 0.09
D = transition duct inlet diameter
d = Preston tube outside diameter
d^+ = normalized Preston tube outside diameter, (dU_τ/ν)
H_{12} = first boundary-layer shape factor, (δ_1/δ_2)
H_{32} = second boundary-layer shape factor, (δ_3/δ_2)
k = turbulence kinetic energy
L = pipe length
P = static pressure
P_i = inlet static pressure
P_w = wall static pressure
R = inlet pipe radius
Re = Reynolds number, (U_bD/ν)
r = radial coordinate
s = peripheral curvilinear coordinate
U, V, W = mean velocity components in the x, y, and z directions, respectively
U^+ = normalized U component, (U/U_τ)
U_b = bulk mean velocity
U_τ = friction velocity, $(\sqrt{\tau_w/\rho})$
u', v', w' = rms normal Reynolds stress components in the x, y, and z directions, respectively
$\overline{u^2}, \overline{v^2}, \overline{w^2}$ = Reynolds normal stress components
$\overline{uv}, \overline{uw}, \overline{vw}$ = Reynolds shear stress components
V_r = resultant transverse velocity vector in the y-z plane, $(V^2 + W^2)^{1/2}$
x, y, z = primary Cartesian coordinates
x' = streamwise coordinate measured from pipe inlet
y^+ = normalized y coordinate, (yU_τ/ν)
δ = boundary-layer thickness
δ_1 = axisymmetric displacement thickness
δ_2 = axisymmetric momentum thickness
δ_3 = axisymmetric energy thickness
ε = dissipation rate of turbulence kinetic energy
η = exponent of superellipse equation
κ = von Karman's constant, 0.41
μ = molecular viscosity
μ_t = turbulent viscosity
ν = kinematic viscosity, (μ/ρ)
ρ = density
τ_w = wall shear stress

Introduction

THE term transition duct refers to a class of internal flow configurations in which the cross-sectional shape changes in the streamwise direction. These configurations include square-to-rectangular ducts, which are used in air conditioning and other low-speed applications. Experimental work in this area has shown that the pressure loss coefficient of a duct with the same inlet and outlet areas is particularly sensitive to the inlet boundary-layer thickness and outlet aspect ratio.[1] Other types of transition ducts include those that have a circular inlet, a rectangular outlet, and a 90-deg bend in the streamwise direction, with increasing cross-sectional area downstream of the inlet to simulate a hydraulic turbine draft tube. Turbulent flow in this particular configuration has been analyzed recently by means of a two-equation (k-ε) turbulence model, both with and without swirl at the inlet.[2,3] The numerical results show that mass flow averaged static pressure recovery is predicted well for swirl intensities as high as 0.5, where the swirl intensity is defined as the ratio of angular momentum flux to axial momentum flux. Square-to-circular ducts constitute still another type of transition duct used in aircraft intake applications. Laser Doppler anemometer (LDA) type data have been taken for subsonic flow in this configuration that demonstrate mean velocity and Reynolds stress behavior in a duct with decreasing cross-sectional area in the streamwise direction.[4]

Presented as Paper 90-1505 at the AIAA 21st Fluid Dynamics, Plasma Dynamics, and Lasers Conference, Seattle, WA, June 18–20, 1990; received Nov. 28, 1990; revision received March 15, 1991; accepted for publication March 15, 1991.

*Graduate Research Assistant; currently Aerospace Engineer, NASA Lewis Research Center, Cleveland, OH 44135. Member AIAA.
†Professor, Department of Mechanical Engineering. Member AIAA.

In aircraft engine exhaust applications, a transition duct is needed between the engine and nozzle when the nozzle has a rectangular cross section. An example of this type of nozzle is the two-dimensional/convergent-divergent (2-D/C-D) multifunction nozzle, which provides thrust vectoring and reversing capabilities in a simple and efficient package.[5] In order to predict the performance of this type of nozzle, flow exiting from the transition duct must be known in sufficient detail, so that inlet conditions at the nozzle entrance are well posed. The transition duct can have either an annular or circular cross section at the inlet, depending on the particular application under consideration. For an annular-to-rectangular transition duct, the effect of inlet swirl on vortex patterns at the duct exit has been examined both experimentally and computationally.[6] Other studies have focused on incompressible swirling and nonswirling flow within a circular-to-rectangular (CR) transition duct.[7-12]

The earliest study of CR transition ducts was an experimental investigation by Mayer.[7] His results showed that the length of the transition section is influential on flow development and that pressure-driven crossflows can lead to significant distortion of the primary flow. Burley et al.[8,9] performed pressure loss tests on five different CR transition ducts in order to determine the effects of duct length, wall shape, and cross-sectional area distribution on performance. Their results show that large regions of separated flow are present whenever the length-to-diameter ratio is < 0.75 and that swirling the flow can have a positive effect on performance for low nozzle pressure ratios. Patrick and McCormick[10,11] were the first to make turbulence measurements within a CR transition duct. Laser Doppler velocimetry (LDV) and total pressure measurements were made at the inlet and outlet planes of two different duct configurations. Results for the relatively short AR310 duct showed that the axial mean velocity in the core region did not develop uniformly but had a convex profile along the major axis at the duct exit plane. Flow at the exit plane of the longer AR630 duct was much more uniform, and a pair of discrete vortices along the duct sidewalls, centered about the duct semimajor axis, was observed. The most recent experimental study of CR transition ducts was conducted by Miau et al.,[12] who examined flow in three ducts with different length-to-diameter ratios. Their results show that the generation of streamwise vorticity is due primarily to transverse pressure gradients induced by geometrical changes in duct shape.

In the present paper, experimental results for a CR transition duct are presented that demonstrate mean flowfield and Reynolds stress behavior within the duct. This study was pursued in order to generate more detailed information on the local flow structure in this type of duct in comparison to that available from earlier studies. The results include data in the near-wall region in order to investigate the adequacy of using wall functions for prediction purposes. The results are intended not only to provide insight into the physics of the flow, but also to serve as a basis for testing turbulence models applicable to this type of flow situation. On the basis of previous work in this area, it was anticipated that skew-induced (pressure-driven) secondary flow would have a dominating influence on the primary flow and on the local turbulence structure.

Experimental Program

Test Section

The particular CR duct configuration chosen for the present study has an exit aspect ratio of 3.0 and a transition length of 1.5 inlet diameters over which changes in cross-sectional shape occur. At each streamwise location, the cross-sectional configuration is defined by the equation of a superellipse, namely, $(y/a)^{\eta} + (z/b)^{\eta} = 1$, where a, b, and η are functions of the streamwise coordinate x. For the selected duct configuration, the ratio of the local cross-sectional area relative to

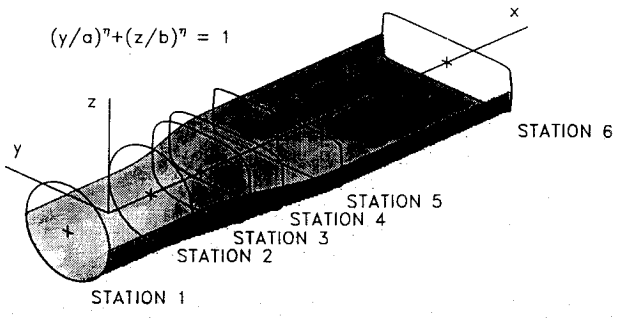

Fig. 1 Circular-to-rectangular duct configuration.

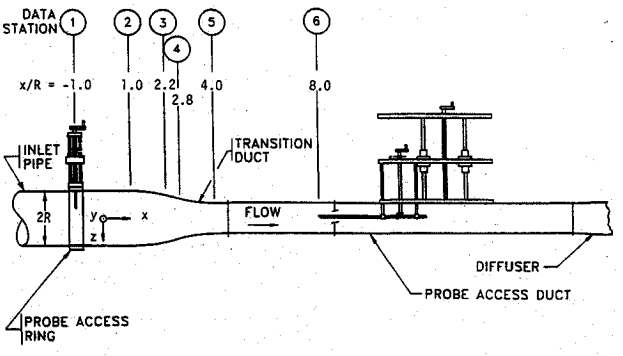

Fig. 2 Schematic of wind tunnel in vicinity of duct.

the inlet area increases from unity at the inlet to a maximum of 1.15 near the midpoint of transition before decreasing back to unity at the duct exit. Flow visualization studies conducted at NASA Lewis Research Center have shown that the flow remains wholly attached within this configuration for subsonic flow in the presence of adverse pressure gradients induced by the 15% area expansion. In reference to Fig. 1, data were taken at stations 1–6, where station 1 is 1 inlet diameter upstream of the start of transition (station 2). Stations 3 and 4 are in the midregion of transition, station 5 is at the end of transition, and station 6 is 2 inlet diameters downstream from the end of transition. The overall length of the duct is 4.5 inlet diameters, with a flanged juncture between stations 5 and 6. The duct was made in half sections of molded epoxy resin fiberglass with a smooth interior surface and had flanges for the purpose of joining the two halves together. More complete details and coordinate specifications of the duct are given in Ref. 13.

Flow Facility

Flow through the transition duct was investigated using the low-speed, open-loop flow facility described by Davis.[13] Atmospheric air, nominally at 293 K, enters the wind tunnel through a 2.8:1 bell-mouth inlet and passes through a settling chamber with a filter/honeycomb flow straightener and two fine mesh screens. The flow then enters a 20:1 contraction, which was designed to provide a uniform, low turbulence level, axisymmetric exit flow using design criteria developed by Morel.[14] From the 20:1 contraction, the flow enters a 20.42-cm-diam straight pipe, 184 cm in length ($L_{pipe}/D = 9$). A 2.54-cm-wide strip of no. 36 sandpaper located 1.3 cm downstream of the pipe inlet serves as a boundary-layer trip. A schematic of the wind tunnel downstream of the pipe is shown in Fig. 2. A probe access ring was located at the end of the pipe section to facilitate detailed measurements of the transition duct inlet flow at station 1. Downstream of the transition duct, the flow enters a rectangular duct that supports the probe traversing mechanism. Air is drawn through the facility by means of a two-speed centrifugal fan. The fan discharges the air back into the laboratory through a set of remotely actuated shutters, which provide a means for varying the mass

flow rate through the wind tunnel. For the experiments reported in this paper, the axial bulk velocity was fixed at 30 mps, corresponding to an inlet bulk Reynolds number of 3.9×10^5.

The origin of the xyz coordinate system shown in Fig. 2 lies midway between stations 1 and 2. This position was used to specify the behavior of $a(x)$, $b(x)$, and $\eta(x)$ in the superellipse equation for the duct cross section. The coefficients of the fifth-order polynomials that model the behavior of $a(x)$, $b(x)$, and $\eta(x)$ are given by Davis.[13] In this paper, results based on pressure probe and hot-wire data obtained at stations 1, 5, and 6 are presented. At station 1, the probes were inserted through the duct wall normal to the axial centerline. At stations 5 and 6, the probes were held parallel to the axial centerline by means of a probe traversing mechanism located downstream of the test section, as shown in Fig. 2. This mechanism was used to translate a probe in the y and z directions and to rotate the probe about its longitudinal axis by means of a spring-loaded (antibacklash) bevel gear arrangement. Dial indicators were used to position the probes in each direction to within an estimated accuracy of ± 0.025 mm, and probes were rotated to a fixed angular position to within an estimated accuracy of ± 0.5 deg.

Pressure Probe Instrumentation

The test section was outfitted with both static and total pressure instrumentation. Static pressure along the periphery of the duct at each station was sampled by means of 0.508-mm-diam wall taps connected to a type J, 48 port Scanivalve. Static pressure along the duct centerline was measured with a 1.5-mm-diam pitot-static probe. Boundary-layer profiles were measured with flattened pitot tubes having outer dimensions of 0.81×0.41 mm at the tip. All pressure data were measured by means of a 10-Torr Barocel electronic manometer, Model 571D-10T-1C2-V1, connected to a Datametrics Model 1174 digital display unit.

Local wall shear stress measurements were made by means of different-diameter Preston tubes resting on the duct wall. At station 1, four tubes with outside diameters of 2.77, 3.96, 5.54, and 6.35 mm were used. At station 5, data were taken with four tubes having outside diameters of 1.07, 1.65, 2.11, and 3.07 mm, and at station 6, two tubes with outside diameters of 1.65 and 2.11 mm were used. The Preston tube data were reduced by means of tabulated calibration data presented by Head and Vasanta Ram.[15] This method of evaluating wall shear stress presumes that the two-dimensional form of the law of the wall is valid and that streamwise pressure gradients are small. It was anticipated that this method would be applicable to data taken at stations 1, 5, and 6, inasmuch as there is no longitudinal wall curvature or cross-sectional area change at these locations.

Hot-Wire Instrumentation

The hot-wire results for stations 5 and 6 are based on the single-wire probe rotation technique developed by Al-Beirutty et al.[16] This technique applies for flows with turbulence levels as high as 50% and allows the mean velocity and Reynolds stress fields to be determined with high accuracy when the mean flow is arbitrarily skewed in pitch and yaw by as much as 20 deg relative to the probe rotation axis. For measurements at station 1, where probes were inserted normal to the duct centerline, the response equations developed by Al-Beirutty et al.[16] were rewritten relative to a coordinate system in which flow skewness is defined relative to a plane normal to the axis of probe rotation.[13] Both techniques are based on the sequential use of slant and normal-wire probes. The prongs of these probes were similar in design to configurations recommended by Comte-Bellot et al.[17] for minimizing aerodynamic interference effects. The sensing element of each probe was a 4-μ-diam, platinum-plated tungsten wire, which was copperplated at both ends to facilitate soldering to the probe tips. The active sensing length of the wire was typically 1 mm relative to a total length of approximately 4 mm between probe tips. The probes were energized by means of a TSI IFA100 constant temperature anemometer. The analog output from the anemometer was digitized by means of a TSI IFA200 A/D converter and recorded on a microVAX workstation where the flow quantities of interest were computed. The sampling rate was 10 kHz and the duration time for analog-to-digital conversion was 15 s.

The sensitivity coefficients for the cooling velocity relation were prescribed as follows. The binormal cooling coefficient h was specified as 0.9 on the basis of calibration data obtained by Arterberry.[18] The tangential cooling coefficient k was obtained by calibrating the slant-wire probe in fully developed pipe flow. A typical value for k was found to be 0.15. At station 1, the probe was calibrated in the low turbulence intensity core flow near the duct centerline. A pitot probe and the wall static pressure were used to determine a reference velocity. For measurements at stations 5 and 6, the probes were calibrated near the axial centerline in the probe access duct (see Fig. 2) with a pitot-static probe providing the reference velocity. The calibrations were performed before and after each run and at time intervals of 3–4 h for longer runs.

Uncertainty Estimates

Results presented in this paper are based on measurements with surface static pressure taps, static pressure probes, total pressure probes, and hot-wire anemometry. The uncertainty estimates quoted for a particular variable represent error bounds associated with the peak value observed for that variable. Uncertainties associated with the pressure probe measurements are based on data presented by Chue.[19] Static pressure coefficient C_p values based on wall tap readings and the static pressure probe are estimated to be accurate to within ± 0.002. Skin-friction coefficient C_f values deduced from Preston tube data at stations 1, 5, and 6 are estimated to be accurate to within ± 0.0001, ± 0.0005, and ± 0.0002, respectively. The estimated accuracy of the normalized velocity component $U^+ = U/U_\tau$ based on total pressure probe data is ± 0.2, ± 0.7, and ± 0.3 at stations 1, 5, and 6, respectively.

The uncertainties in hot-wire-based results were estimated from an error analysis presented by Al-Beirutty.[20] In that analysis, the effects of uncertainties in the slant-wire angle α, binormal and tangential cooling coefficients h and k, normal and slant-wire calibration intercept values $E_{0,n}$ and $E_{0,s}$, slant-wire calibration slope B_c, and the measured normal and slant-wire voltages $\overline{E_n}$, $\overline{E_s}$, $\overline{e_n^2}$ and $\overline{e_s^2}$ are taken into account. If the above considerations are applied to the present results, then the uncertainties in hot-wire-based values of U/U_b and V/U_b are estimated as ± 0.01 and ± 0.002, respectively. Uncertainties in the Reynolds stress components $\overline{u^2}/U_b^2$, $\overline{v^2}/U_b^2$, $\overline{w^2}/U_b^2$, $\overline{uv}/U_b^2$, $\overline{uw}/U_b^2$, and $\overline{vw}/U_b^2$ are estimated as ± 0.0001, ± 0.0002, ± 0.0002, ± 0.00015, ± 0.00015, and ± 0.0001, respectively.

Results and Discussion

Station 1 (Inlet Conditions)

Flow at station 1 corresponds to partially developed turbulent pipe flow. Mean velocity profiles measured along four equally spaced radial traverses ($n = 1, 2, 3, 4$) at this station are shown in Fig. 3 in terms of law-of-the-wall coordinates. The excellent peripheral symmetry of the flow and agreement with law-of-the-wall behavior are readily apparent. The d^+ value corresponding to the outside diameter of each Preston tube is also shown in Fig. 3. The largest tube extended slightly into the wake region and, as a result, skin-friction values deduced from this tube were slightly higher than those measured by the three smallest tubes. Friction velocities deduced from the three smallest tubes deviated by <0.3% from their mean value. This value was used to normalize the results shown in Fig. 3.

Reynolds normal and shear stress distributions measured at station 1 are shown in Figs. 4a and 4b, respectively. Ex-

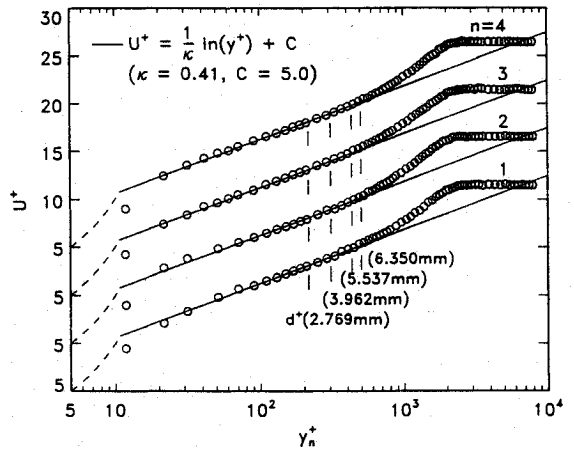

Fig. 3 Law-of-the-wall velocity profiles at station 1.

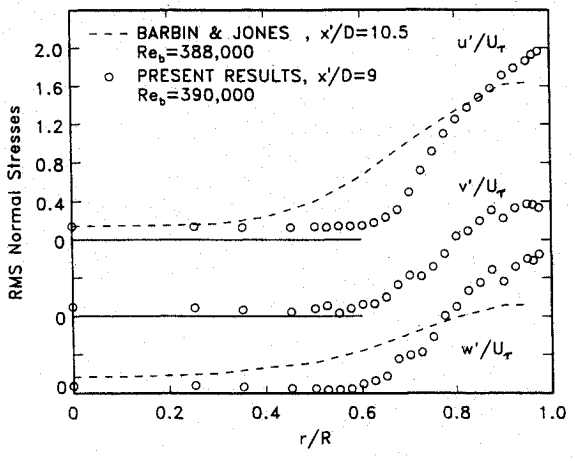

a) RMS normal stress components

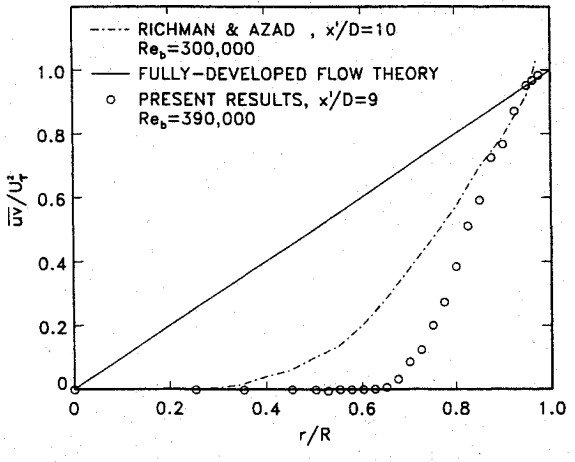

b) Shear stress component

Fig. 4 Reynolds stress distributions at station 1.

perimental results reported by Barbin and Jones[21] and Richman and Azad[22] at approximately the same streamwise location and operating Reynolds number are also shown for purposes of comparison. It can be seen that the stress distributions of Refs. 21 and 22 begin to deviate from near-zero levels in the core flow at radial positions farther from the wall than the radial position where results referred to the present study begin to deviate (near $r/R = 0.6$). This comparison indicates that the boundary layer developed more rapidly within the pipes used by Refs. 21 and 22 than in the one used in the present study. This result is not unexpected because Klein[23] has shown that boundary-layer growth within a pipe is extremely sensitive to entrance and upstream flow conditions. Contraction ratio, boundary-layer tripping devices, and starting conditions (continuous flow vs bypass bleed) all influence local flow development downstream of the pipe inlet.

Table 1 Flow conditions at station 1

δ/R	0.2855
δ_1/R	0.0383
δ_2/R	0.0281
δ_3/R	0.0497
B	0.0765
H_{12}	1.364
H_{32}	1.771
$\tau_w/\tau_{w,FD}$	0.96
u'/U_{cl}	0.003
R, cm	10.214

The more rapid boundary-layer growth associated with Richman and Azad's[22] experiments can probably be attributed to the wider sandpaper tripping device used in their study, which extended over a streamwise width of 0.9 pipe diameters in comparison to the width used in the present study (0.12 pipe diameters). In Barbin and Jones'[21] experiments, a sand-grain tip of the same relative width as that used in the present study was employed. Bypass bleed through an annular gap between the pipe and a 4:1 contraction ratio nozzle was used to promote spanwise flow uniformly across the pipe inlet. In reference to Fig. 1 of Ref. 21, the pipe in Barbin and Jones' experiments extended upstream into the nozzle, so that the pipe inlet may have been at a streamwise location where streamlines within the nozzle were still converging. Under these conditions, flow at the pipe inlet would not have been parallel to the pipe surface and the flow may have separated at the wedge-shaped lip of the pipes. This event, if it occurred, could have promoted more rapid boundary-layer growth in comparison to that observed in the present study. If local flow separation and reattachment did occur near the pipe inlet in Barbin and Jones' experiments, then one would also anticipate that flow in the near-entrance region would not be in local equilibrium. This conjecture is supported to some extent by the behavior of velocity profiles measured by Barbin and Jones at $x'/D = 1.5$, 4.5, and 7.5, all of which show significant departures from the law of the wall in the inner region of the boundary layer (refer to Fig. 6 of Ref. 21).

The differences between corresponding distributions in Figs. 4a and 4b could be reconciled further if a code were available for predicting developing turbulent pipe flow with high accuracy starting from a low-turbulence level, uniform inlet flow condition. Unfortunately, predictions of a given variable in the entrance region based on various turbulence models show differences that are of the same order of magnitude as those that exist among the various data sets for nominally the same operating conditions.[23-25] Further work will be required in order to 1) provide comprehensive data that characterize disturbance-free, turbulent boundary-layer growth in a circular pipe, and 2) develop a code that can predict this behavior, recognizing that the data may still need to be corrected for virtual origin (streamwise displacement) effects. It should be noted here that the present data set at station 1 appears to be relatively free of upstream disturbances, inasmuch as the core flow at this location is uniform and at a relatively low turbulence level (0.3%, as indicated in Table 1) and velocity profiles measured along four radial traverses 90 deg apart are symmetric and in excellent agreement with the law of the wall (refer to Fig. 3).

Stations 5 and 6

As noted earlier, station 5 coincides with the end of transition (end of cross-sectional shape change) and station 6 is located 2 inlet diameters downstream from station 5. Reference coordinates applicable to both stations are shown in Fig.

5. Symmetry was assumed about the vertical midplane $y = 0$ and, as such, data were taken only in the half duct section shown in Fig. 5. Rather than assuming symmetry about the horizontal midplane $z = 0$, hot-wire measurements were made in both quadrants 1 and 2 shown in Fig. 5. All subsequent contour results are based on data obtained in both quadrants, so that the level of symmetry about the midplane $z = 0$ is a direct indication of the quality of the flow and of the measurement techniques employed in this study. Data were taken at selected points on a 63 × 19 rectangular grid in each quadrant. The spacing between data points varied from 2.54 cm in the core region to 0.254 cm in regions of large gradients. Approximately 400 data points were used at each station. For plotting purposes, the remainder of the data mesh was filled in by means of a monotonic derivative spline interpolant.[26]

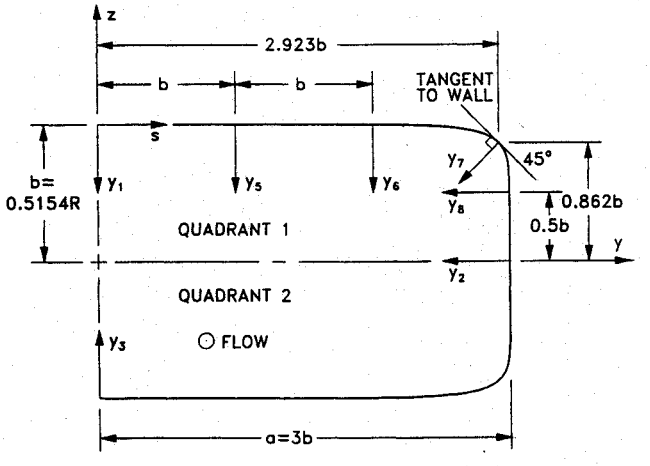

Fig. 5 Reference coordinates for stations 5 and 6.

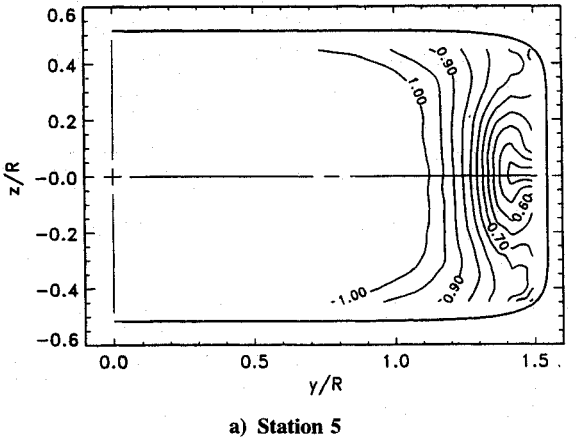

a) Station 5

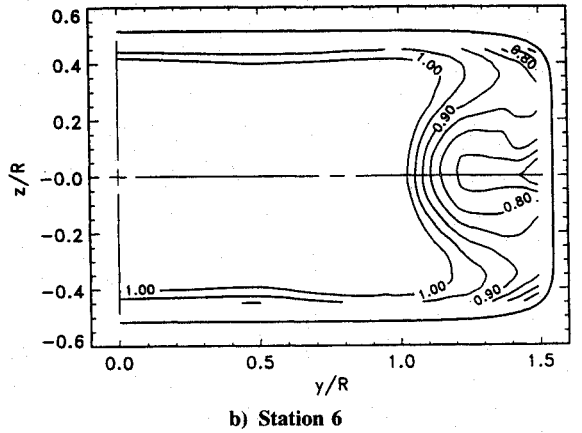

b) Station 6

Fig. 6 Axial mean velocity (U/U_b) contours.

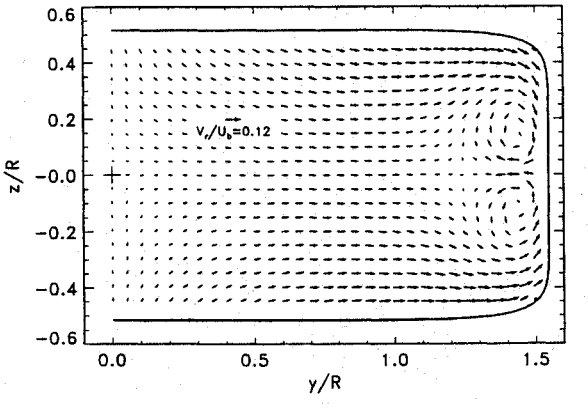

a) Station 5

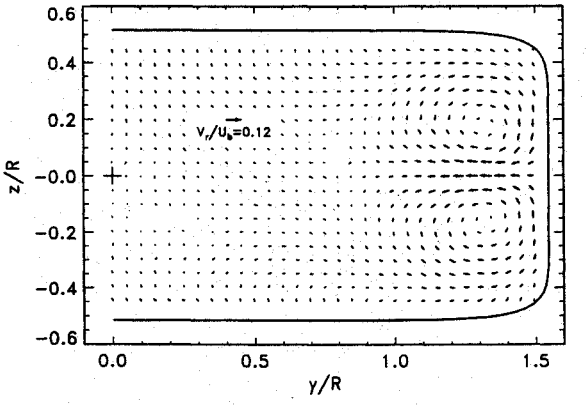

b) Station 6

Fig. 7 Transverse mean velocity (V_r/U_b) vectors.

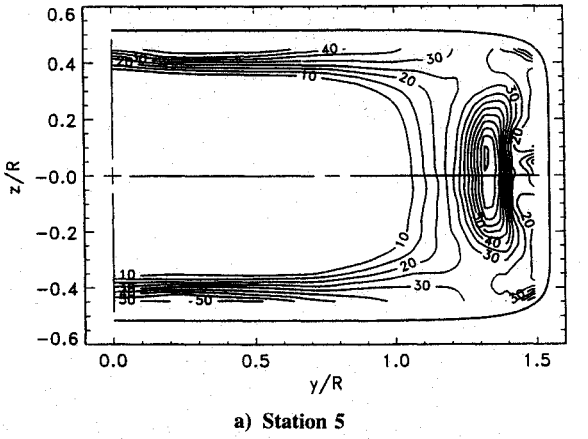

a) Station 5

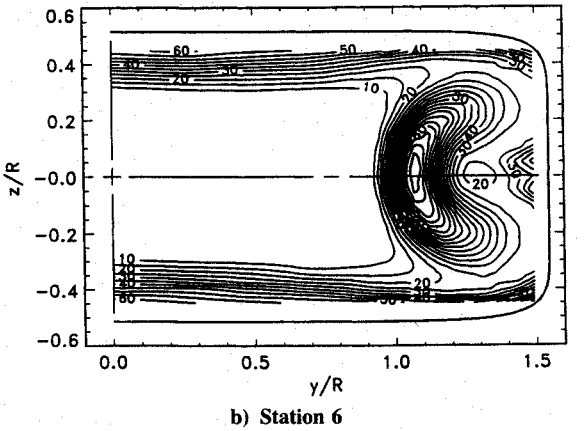

b) Station 6

Fig. 8 Reynolds normal stress ($\overline{u^2}/U_b^2 \times 10^4$) contours.

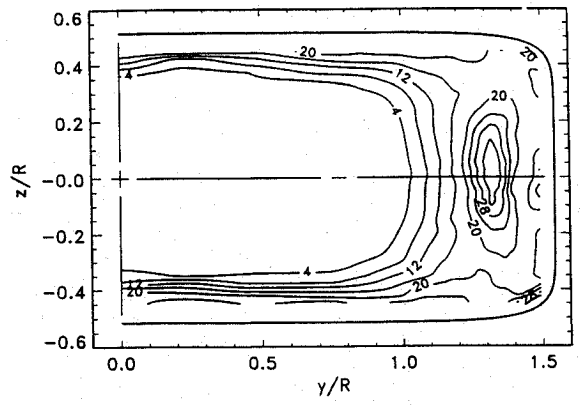

a) Station 5

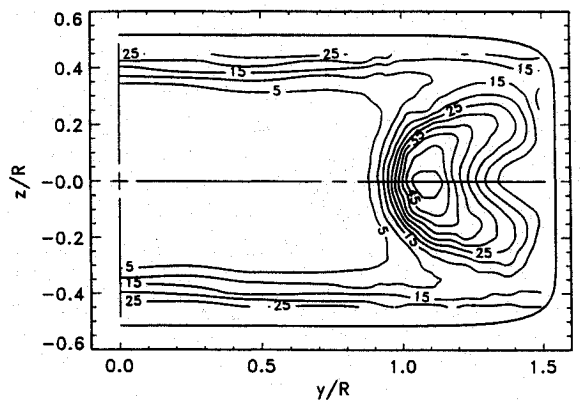

b) Station 6

Fig. 9 Reynolds normal stress ($\overline{v^2}/U_b^2 \times 10^4$) contours.

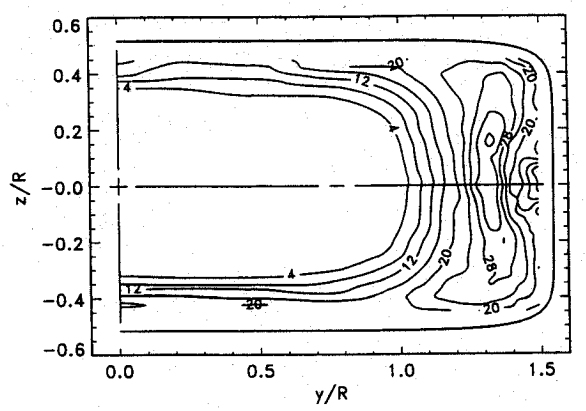

a) Station 5

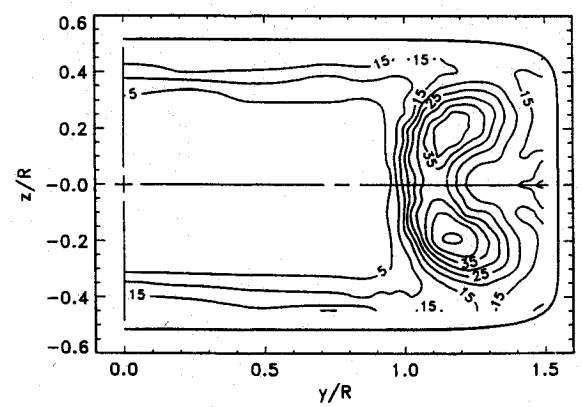

b) Station 6

Fig. 10 Reynolds normal stress ($\overline{w^2}/U_b^2 \times 10^4$) contours.

This method of interpolation performs no smoothing and guarantees no overshoot of the data.

Axial mean velocity contours measured at stations 5 and 6 are shown in Fig. 6. Transverse velocity vectors measured at these same locations are shown in Fig. 7. In reference to Fig. 6, it can be seen that axial mean velocity contours are symmetrically distorted about the midplane $z = 0$ in the vicinity of the duct sidewall. This distortion is caused by a secondary flow vortex pair, which is centered about the midplane, as shown in Fig. 7. These vortices arise as a result of lateral (z-direction) skewing of the near-wall flow in the vicinity of the sidewall induced by transverse pressure gradients generated by changes in wall curvature. At station 5, the vortices are oblong in shape and their centers are positioned relatively near the duct sidewall. At station 6, the vortices have grown in lateral extent, are more circular, and are centered farther away from the sidewall. The axial mean velocity contours at stations 5 and 6 indicate that boundary-layer profiles normal to the duct sidewall in the vicinity of the midplane $z = 0$ exhibit double inflection behavior. This is a result of the vortex pair convecting a ridge of high momentum fluid from the core to this region along the duct sidewalls. A break in the ridge occurs at the midplane due to a transfer of low-momentum fluid from the boundary layer toward the axial centerline, creating a flat spot in the velocity field. This flat region is seen to be much larger at station 6 than at station 5.

Reynolds stress contours for all six stress components at stations 5 and 6 are shown in Figs. 8–13. Negative contour levels are represented by dashed lines. The level of symmetry for each stress component about the midplane $z = 0$ is very good, even for the difficult-to-measure $\overline{vw}$ stress component shown in Fig. 13. As expected, the $\overline{uw}$ and $\overline{vw}$ stress components change sign between quadrants 1 and 2. In general, Figs. 8–13 show that the Reynolds stress contours are more distorted at station 6 than at station 5 and that peak contour

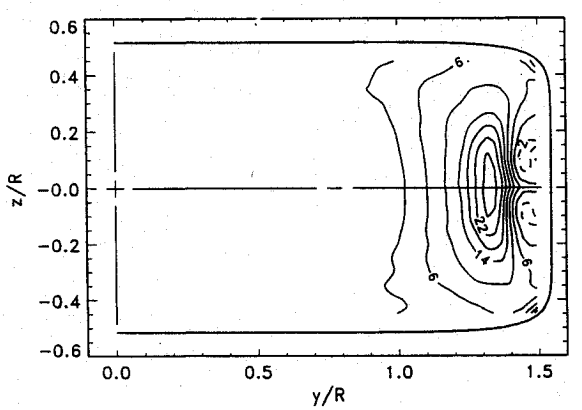

a) Station 5

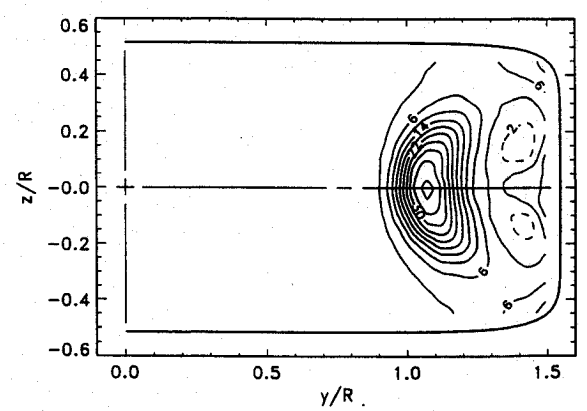

b) Station 6

Fig. 11 Reynolds shear stress ($\overline{uv}/U_b^2 \times 10^4$) contours.

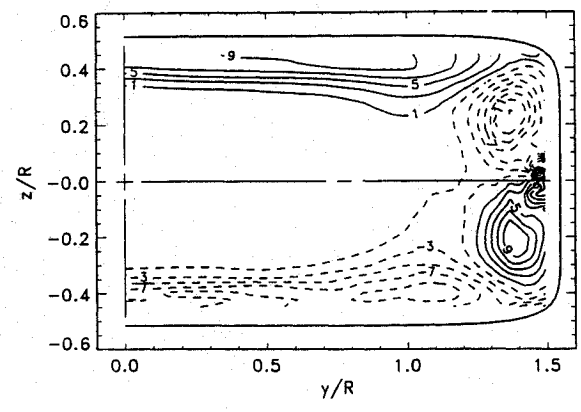

a) Station 5

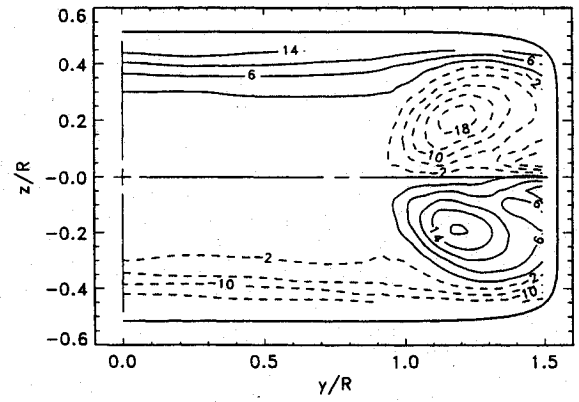

b) Station 6

Fig. 12 Reynolds shear stress ($\overline{uw}/U_b^2 \times 10^4$) contours.

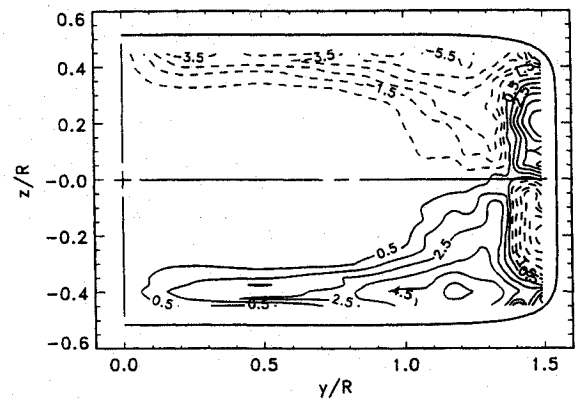

a) Station 5

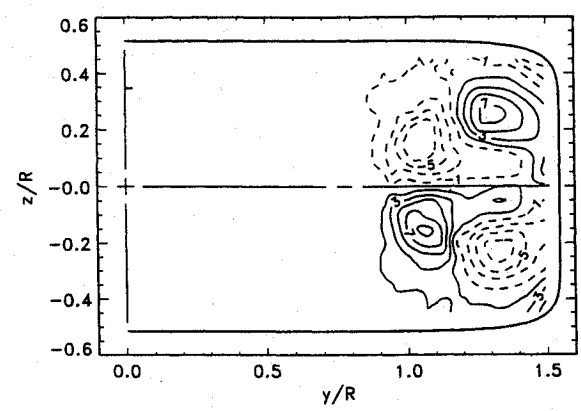

b) Station 6

Fig. 13 Reynolds shear stress ($\overline{vw}/U_b^2 \times 10^4$) contours.

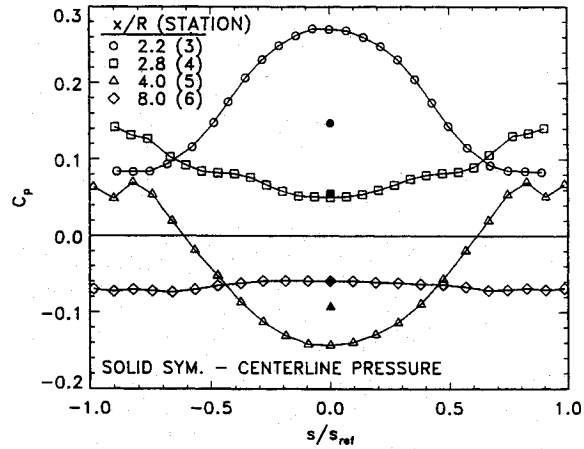

Fig. 14 Peripheral wall pressure coefficient distributions.

values are displaced farther from the duct sidewall. At both stations, the peak values of the transverse normal stress components $\overline{v^2}$ and $\overline{w^2}$ are nearly equal and are roughly half the peak value of the streamwise normal stress component $\overline{u^2}$. At station 6, the $\overline{w^2}$ stress component exhibits a double peak behavior. The sign of the $\overline{uv}$ and $\overline{uw}$ shear stress components is compatible with the sign of the primary rate of strain components $\partial U/\partial y$ and $\partial U/\partial z$ deduced from the contour plots of axial mean velocity shown in Fig. 6. This is true even for the small pockets of negative $\overline{uv}$ shear stress, which are a result of a positive mean rate of strain ($\partial U/\partial y > 0$) associated with the aforementioned velocity ridge. Along the midplane $z = 0$ where the axial mean velocity profile flattens, the primary mean rate of strain in both the y and z directions is nearly zero and, as a result, shear stress levels in this region are depressed.

Wall Static Pressure Distributions

Peripheral wall static pressure coefficient distributions measured at stations 3–6 are shown in Fig. 14. In this figure, s is a peripheral wall coordinate, defined in Fig. 5, and s_{ref} is one-quarter of the duct periphery at each data station. Solid symbols represent static pressure measured along the axial centerline of the duct. The excellent spanwise regularity at all stations supports the assumption of symmetry about the vertical midplane $y = 0$. In general, local wall static pressure is a function of cross-sectional area, wall curvature, and viscous forces in the flow. Station 3 is located at an axial position where streamwise diffusion of the flow is occurring (refer to Fig. 1). This results in a net rise in static pressure above the inlet value ($C_p = 0$), which is reflected in the centerline pressure. Concave curvature along the upper wall induces a positive pressure gradient ($\partial P/\partial r > 0$), which results in an observed pressure peak at $s/s_{ref} = 0$. Conversely, convex wall curvature along the sidewalls induces a negative pressure gradient, resulting in the pressure minima at $s/s_{ref} = \pm 1$. A net decrease in static pressure occurs between stations 3 and 4, which is the result of a slight decrease in cross-sectional area and viscous losses. Also, the radius of curvature of the walls changes sign between stations 3 and 4, which causes maximum and minimum pressures to occur along the side and upper walls, respectively. At station 5, the cross-sectional area has returned to the inlet value, so that a net decrease in pressure relative to the inlet occurs, which is due only to viscous effects. Although there is no streamwise curvature of the walls at this station, upstream curvature effects are still strongly present (wall curvature peaks between stations 4 and 5). It can also be seen that undulations exist in the distributions near the center of the sidewalls at station 5 (near $s/s_{ref} = \pm 1$), which are undoubtedly due to the vortex pair that is in close proximity (refer to Fig. 7a). At station 6, no area change or curvature effects are present, so that the static pressure is nominally constant across the entire duct cross section.

Wall Function Behavior

The use of wall functions for predicting the present flow was analyzed. Skin-friction coefficient distributions deduced from Preston tube data at stations 5 and 6 are shown in Fig. 15. These data were taken along the periphery of the duct that bounds quadrant 1, defined as shown in Fig. 5. The results based on data obtained with different diameter Preston tubes at station 5 show systematic variations with a change in diameter, particularly for $s/s_{ref} < 0.6$, indicating that either deviations from the law of the wall exist in this region or that some of the Preston tubes extended beyond the log-law region. Boundary-layer profiles were measured along the y_n traverses shown in Fig. 5 ($n = 1, 2, 5, 6, 7, 8$) with both pitot and hot-wire probes. Results obtained at stations 5 and 6, plotted in law-of-the-wall coordinates, are shown in Fig. 16. The friction velocities used for these plots are based on the average distribution lines shown in Fig. 15. The d^+ value corresponding to the outside diameter of each Preston tube is also shown superimposed on these plots. At station 5, deviations from the law of the wall are apparent for y^+ values > 80. In the near-wall region, however, all profiles exhibit law-of-the-wall behavior within the interval $30 \leq y^+ \leq 80$. At station 6, the law of the wall is satisfied on all traverses for y^+ values between 30 and 200. This behavior implies that the law of the wall may be used as a wall function for prediction purposes, recognizing that the limiting y^+ value on the first mesh line between the duct inlet (station 1) and station 5 may be less than the limiting value that applies at station 5 ($y^+ \cong 80$).

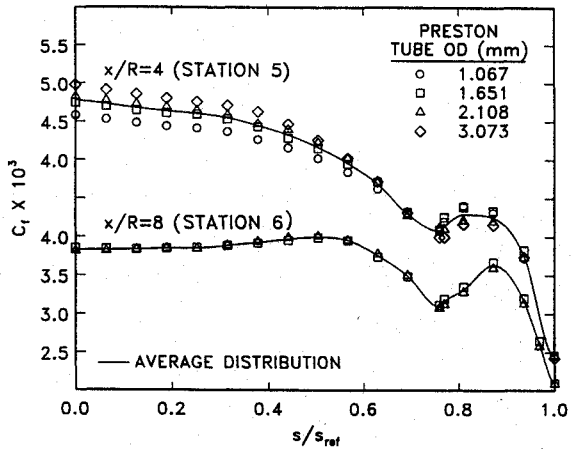

Fig. 15 Peripheral skin-friction coefficient distributions.

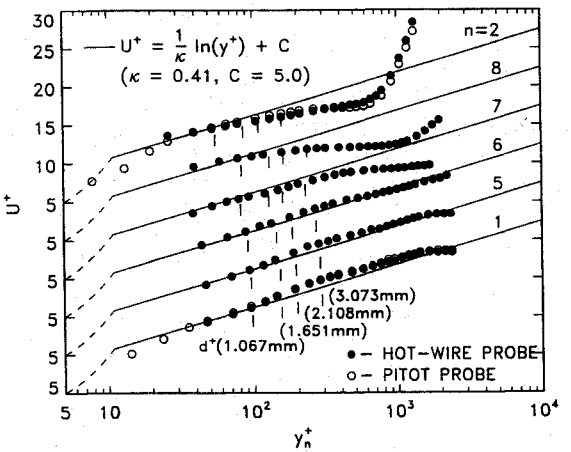

a) Station 5

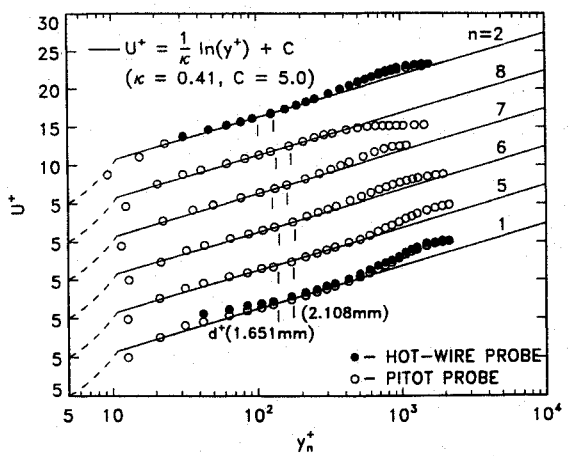

b) Station 6

Fig. 16 Law-of-the-wall velocity profiles.

Wall function behavior for the turbulence kinetic energy k was also analyzed. Distributions of k/U_τ^2 measured along several traverses normal to the horizontal midplane $z = 0$ at stations 5 and 6 are shown in Fig. 17. The conventional value of the wall function for k, namely, $k/U_\tau^2 = 1/\sqrt{C_\mu}$ with $C_\mu = 0.09$, is also shown on this plot. Although the results are restricted to y^+ values > 400 because of limitations imposed by the probe rotation mechanism, some conclusions can still be drawn. For example, it can be seen that distributions measured along the vertical midplane traverse $y/R = 0$ at stations 5 and 6 both tend toward the conventional limit. This same comment applies for all other distributions measured at station 6. At station 5, however, the trends are more difficult to discern, especially along the traverse $y/R = 1.37$, which lies within the sidewall boundary layer.

The behavior of k/U_τ^2 along the horizontal midplane traverse $z = 0$ at stations 5 and 6 is shown in Fig. 18. The peak in the distribution measured at station 6 is displaced farther from the sidewall than the peak in the distribution measured at station 5 because of the convecting action of the vortex pair between these two stations. It can be seen that the distribution measured at station 6 approaches the conventional limit but the distribution measured at station 5 does not. The first data point at station 5 is at $y_2^+ \cong 300$, however, which is well beyond the region where law-of-the-wall behavior applies (refer to the y_2^+ distribution for station 5 in Fig. 16a).

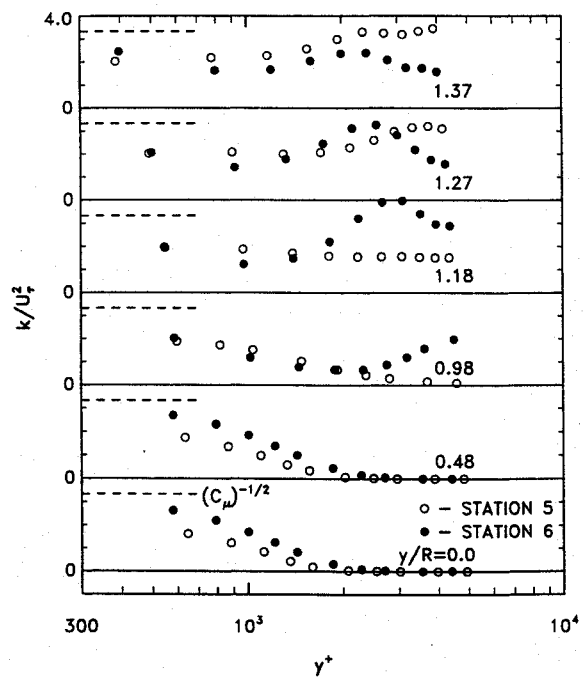

Fig. 17 Turbulence kinetic energy (k/U_τ^2) distributions normal to the midplane $z = 0$.

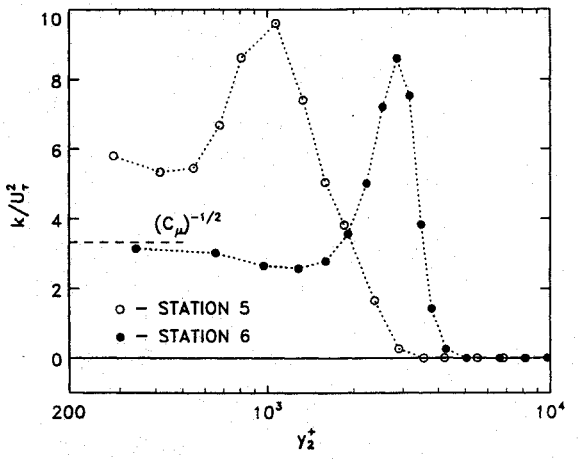

Fig. 18 Turbulence kinetic energy (k/U_τ^2) distributions along the midplane $z = 0$.

In reference to predictions, if y^+ on the first mesh line is restricted to an interval between 30 and 50, then k/U_τ^2 on this mesh line may be close to the conventional limit at station 5 and, indeed, at intermediate stations within the duct where streamwise changes in wall curvature are occurring. Further measurements in the near-wall region will be required in order to determine whether the conjectured behavior exists within this present duct configuration.

Concluding Remarks

Incompressible, turbulent, swirl-free flow through a circular-to-rectangular transition duct has been studied experimentally. Inlet conditions to the duct correspond to partially developed turbulent pipe flow. The three mean velocity components and the six Reynolds stress components were measured at two axial stations downstream of transition. The results show that a secondary flow vortex pair develops along the duct sidewalls that significantly distorts the primary mean velocity and Reynolds stress fields. Flow in the near-wall region is also modified to the extent that law-of-the-wall behavior is diminished in regions where streamwise wall curvature effects influence the flow. Analysis of the results shows that conventional wall functions, while applicable, must be used with caution in any predictive code applied to the present flow situation.

The data that have been obtained can serve as an experimental data base for computational fluid dynamics code calibration/verification, inasmuch as the results demonstrate the appropriate symmetry and are based on well-defined inlet conditions. The results of this study should also serve as a means of testing various turbulence models that have been proposed for predicting flows in which streamline curvature efforts are important. To facilitate comparison, the transition duct geometric variables and flow data are available on magnetic media from the senior author.

Acknowledgment

The authors would like to express their appreciation to NASA Lewis Research Center, Cleveland, OH, which sponsored this work under Grant NAG 3-376.

References

[1]Dekam, E. I., and Calvert, J. R., "Effects of Inlet Conditions and Surface Roughness on the Performance of Transitions Between Square and Rectangular Ducts of the Same Cross-Sectional Area," *International Journal of Heat and Fluid Flow*, Vol. 8, No. 4, 1987, pp. 287–292.

[2]Vu, T. C., and Shyy, W., "Navier-Stokes Flow Analysis for Hydraulic Turbine Draft Tubes," *Journal of Fluids Engineering*, ASME Transactions, Vol. 112, No. 2, 1990, pp. 199–204.

[3]Agouzoul, M., Reggio, M., and Camarero, R., "Calculation of Turbulent Flows in a Hydraulic Turbine Draft Tube," *Journal of Fluids Engineering*, ASME Transactions, Vol. 112, No. 3, 1990, pp. 257–263.

[4]Taylor, A. M. K. P., Whitelaw, J. H., and Yianneskis, M., "Turbulent Flow in a Square-to-Round Transition," NASA CR-3447, July 1981.

[5]Sevens, H. L., Thayer, E. B., and Fullerton, J. F., "Development of the Multi-Function 2-D/C-D Nozzle," AIAA Paper 81-1491, July 1981.

[6]Sobota, T. H., and Marble, F. E., "Swirling Flows in an Annular-to-Rectangular Transition Section," *Journal of Propulsion and Power*, Vol. 5, No. 3, 1989, pp. 334–340.

[7]Mayer, E., "Effect of Transition in Cross-Sectional Shape on the Development of the Velocity and Pressure Distribution of the Turbulent Flow in Pipes," NACA TM903, Aug. 1939.

[8]Burley, J. R., II, and Carlson, J. R., "Circular-to-Rectangular Transition Ducts for High-Aspect Ratio Nonaxisymmetric Nozzles," AIAA Paper 85-1346, July 1985.

[9]Burley, J. R., II, Bangert, L. S., and Carlson, J. R., "Investigation of Circular-to-Rectangular Transition Ducts for High-Aspect Ratio Nonaxisymmetric Nozzles," NASA TP-2534, March 1986.

[10]Patrick, W. P., and McCormick, D. C., "Circular-to-Rectangular Duct Flows: A Benchmark Experimental Study," SAE TP-871776, Society of Automotive Engineers, Warrendale, PA, Oct. 1987.

[11]Patrick, W. P., and McCormick, D. C., "Laser Velocimeter and Total Pressure Measurements in Circular-to-Rectangular Transition Ducts," NASA CR-182286, June 1988.

[12]Miau, J. J., Leu, T. S., Chou, J. H., Lin, S. A., and Lin, C. K., "Flow Distortion in a Circular-to-Rectangular Transition Duct," *AIAA Journal*, Vol. 28, No. 8, 1990, pp. 1447–1456.

[13]Davis, D. O., "Experimental Investigation of Turbulent Flow Through a Circular-to-Rectangular Duct," Ph.D. Dissertation, Dept. of Mechanical Engineering, Univ. of Washington, Seattle, WA, June 1991.

[14]Morel, T., "Comprehensive Design of Axisymmetric Wind Tunnel Contractions," *Journal of Fluids Engineering*, ASME Transactions, Vol. 97, No. 2, 1975, pp. 225–233.

[15]Head, M. R., and Vasanta Ram, V., "Simplified Presentation of Preston Tube Calibration," *Aeronautical Quarterly*, Vol. 22, Pt. 3, 1971, pp. 295–300.

[16]Al-Beirutty, M. H., Arterberry, S. H., and Gessner, F. B., "A Hot-Wire Technique for Complex Turbulent Flows," *Proceedings of the 1st National Fluid Dynamics Congress*, Pt. 3, AIAA, Washington, DC, 1988, pp. 1479–1486.

[17]Comte-Bellot, G., Strohl, A., and Alcaraz, E., "On Aerodynamic Disturbances Caused by Single Hot-Wire Probes," *Journal of Applied Mechanics*, ASME Transactions, Vol. 38, No. 4, 1971, pp. 767–774.

[18]Arterberry, S. H., "An Improved Method of Flow Field Determination in Three-Dimensional Flows of Low Intensity and Moderate Skewness," M.S. Thesis, Dept. of Mechanical Engineering, Univ. of Washington, Seattle, WA, March 1982.

[19]Chue, S. H., "Pressure Probes for Fluid Measurements," *Progress in Aerospace Sciences*, Vol. 16, No. 2, 1975, pp. 147–223.

[20]Al-Beirutty, M. H., "Development of a Hot-Wire Measurement Technique for Moderate Intensity Three-Dimensional Flows," Ph.D. Dissertation, Dept. of Mechanical Engineering, Univ. of Washington, Seattle, WA, April 1987.

[21]Barbin, A. R., and Jones, J. B., "Turbulent Flow in the Inlet Region of a Smooth Pipe," *Journal of Basic Engineering*, ASME Transactoins, Vol. 85, No. 1, 1963, pp. 29–39.

[22]Richman, J. W., and Azad, R. S., "Developing Turbulent Flow in a Smooth Pipe," *Applied Scientific Research*, Vol. 28, No. 12, 1973, pp. 419–441.

[23]Klein, A., "Review: Turbulent Developing Pipe Flow," *Journal of Fluids Engineering*, Vol. 103, No. 2, 1981, pp. 243–249.

[24]Martinuzzi, R., and Pollard, A., "Comparative Study of Turbulence Models in Predicting Turbulent Pipe Flow, Part I: Algebraic Stress and k-ε Models," *AIAA Journal*, Vol. 27, No. 1, 1989, pp. 29–36.

[25]Pollard, A., and Martinuzzi, R., "Comparative Study of Turbulence Models in Predicting Turbulent Pipe Flow, Part II: Reynolds Stress and k-ε Models," *AIAA Journal*, Vol. 27, No. 12, 1989, pp. 1714–1721.

[26]Fritsch, F. N., and Carlson, R. E., "Piercewise Cubic Interpolation Methods," Lawrence Livermore Lab., UCRL-81230, Livermore, CA, Nov. 1978.